

In vivo three-dimensional optical coherence elastography[◇]

Brendan F. Kennedy,^{1*} Xing Liang,^{2,3} Steven G. Adie,² Derek K. Gerstmann,^{4,5}
Bryden C. Quirk,¹ Stephen A. Boppart,^{2,3,6} and David D. Sampson^{1,4}

¹Optical + Biomedical Engineering Laboratory, School of Electrical, Electronic and Computer Engineering,
The University of Western Australia, 35 Stirling Highway, Crawley, Western Australia 6009, Australia

²Department of Electrical and Computer Engineering, University of Illinois at Urbana-Champaign,
405 North Matthews, Urbana, Illinois 61801, USA

³Beckman Institute for Advanced Science and Technology, University of Illinois at Urbana-Champaign,
405 North Matthews, Urbana, Illinois 61801, USA

⁴Centre for Microscopy, Characterisation and Analysis, The University of Western Australia,
35 Stirling Highway, Crawley, Western Australia, 6009, Australia

⁵iVEC @ The University of Western Australia (iVEC @ UWA), The University of Western Australia,
35 Stirling Highway, Crawley, Western Australia 6009, Australia

⁶Departments of Bioengineering and Medicine, University of Illinois at Urbana-Champaign,
405 North Matthews, Urbana, Illinois 61801, USA

*brendank@ee.uwa.edu.au

Abstract: We present the first three-dimensional (3D) data sets recorded using optical coherence elastography (OCE). Uni-axial strain rate was measured on human skin *in vivo* using a spectral-domain optical coherence tomography (OCT) system providing >450 times higher line rate than previously reported for *in vivo* OCE imaging. Mechanical excitation was applied at a frequency of 125 Hz using a ring actuator sample arm with, for the first time in OCE measurements, a controlled static preload. We performed 3D-OCE, processed in 2D and displayed in 3D, on normal and hydrated skin and observed a more elastic response of the stratum corneum in the hydrated case.

©2011 Optical Society of America

OCIS codes: (110.4500) Optical coherence tomography; (290.5820) Scattering measurements; (170.6935) Tissue characterization.

[◇]Data sets associated with this article are available at <http://hdl.handle.net/10376/1561>.
Links such as “View 1” that appear in figure captions and elsewhere will launch custom data views if ISP software is present.

References and links

1. Y. C. Fung, *Biomechanics: Mechanical Properties of Living Tissue* (Springer-Verlag, 1993).
2. J. F. Greenleaf, M. Fatemi, and M. Insana, “Selected methods for imaging elastic properties of biological tissues,” *Annu. Rev. Biomed. Eng.* **5**(1), 57–78 (2003).
3. M. Fatemi, A. Manduca, and J. F. Greenleaf, “Imaging elastic properties of biological tissues by low-frequency harmonic vibration,” *Proc. IEEE* **91**(10), 1503–1519 (2003).
4. J. Ophir, I. Céspedes, H. Ponnekanti, Y. Yazdi, and X. Li, “Elastography: a quantitative method for imaging the elasticity of biological tissues,” *Ultrason. Imaging* **13**(2), 111–134 (1991).
5. R. Muthupillai, D. J. Lomas, P. J. Rossman, J. F. Greenleaf, A. Manduca, and R. L. Ehman, “Magnetic resonance elastography by direct visualization of propagating acoustic strain waves,” *Science* **269**(5232), 1854–1857 (1995).
6. A. Itoh, E. Ueno, E. Tohno, H. Kamma, H. Takahashi, T. Shiina, M. Yamakawa, and T. Matsumura, “Breast disease: clinical application of US elastography for diagnosis,” *Radiology* **239**(2), 341–350 (2006).
7. A. L. McKnight, J. L. Kugel, P. J. Rossman, A. Manduca, L. C. Hartmann, and R. L. Ehman, “MR elastography of breast cancer: preliminary results,” *AJR Am. J. Roentgenol.* **178**(6), 1411–1417 (2002).
8. D. L. Cochlin, R. H. Ganatra, and D. F. R. Griffiths, “Elastography in the detection of prostatic cancer,” *Clin. Radiol.* **57**(11), 1014–1020 (2002).
9. J. Foucher, E. Chanteloup, J. Vergniol, L. Castéra, B. Le Bail, X. Adhoute, J. Bertet, P. Couzigou, and V. de Lédizinghen, “Diagnosis of cirrhosis by transient elastography (FibroScan): a prospective study,” *Gut* **55**(3), 403–408 (2006).

10. S. A. Kruse, G. H. Rose, K. J. Glaser, A. Manduca, J. P. Felmlee, C. R. Jack, Jr., and R. L. Ehman, "Magnetic resonance elastography of the brain," *Neuroimage* **39**(1), 231–237 (2008).
11. C. L. de Korte, G. Pasterkamp, A. F. W. van der Steen, H. A. Woutman, and N. Bom, "Characterization of plaque components with intravascular ultrasound elastography in human femoral and coronary arteries *in vitro*," *Circulation* **102**(6), 617–623 (2000).
12. J. M. Schmitt, "OCT elastography: imaging microscopic deformation and strain of tissue," *Opt. Express* **3**(6), 199–211 (1998).
13. R. C. Chan, A. H. Chau, W. C. Karl, S. Nadkarni, A. S. Khalil, N. Iftimia, M. Shishkov, G. J. Tearney, M. R. Kaazempur-Mofrad, and B. E. Bouma, "OCT-based arterial elastography: robust estimation exploiting tissue biomechanics," *Opt. Express* **12**(19), 4558–4572 (2004).
14. J. Rogowska, N. A. Patel, J. G. Fujimoto, and M. E. Brezinski, "Optical coherence tomographic elastography technique for measuring deformation and strain of atherosclerotic tissues," *Heart* **90**(5), 556–562 (2004).
15. H. J. Ko, W. Tan, R. Stack, and S. A. Boppart, "Optical coherence elastography of engineered and developing tissue," *Tissue Eng.* **12**(1), 63–73 (2006).
16. R. K. Wang, Z. H. Ma, and S. J. Kirkpatrick, "Tissue Doppler optical coherence elastography for real time strain rate and strain mapping of soft tissue," *Appl. Phys. Lett.* **89**(14), 144103 (2006).
17. S. J. Kirkpatrick, R. K. Wang, and D. D. Duncan, "OCT-based elastography for large and small deformations," *Opt. Express* **14**(24), 11585–11597 (2006).
18. X. Liang, A. L. Oldenburg, V. Crecea, E. J. Chaney, and S. A. Boppart, "Optical micro-scale mapping of dynamic biomechanical tissue properties," *Opt. Express* **16**(15), 11052–11065 (2008).
19. S. G. Adie, B. F. Kennedy, J. J. Armstrong, S. A. Alexandrov, and D. D. Sampson, "Audio frequency *in vivo* optical coherence elastography," *Phys. Med. Biol.* **54**(10), 3129–3139 (2009).
20. B. F. Kennedy, T. R. Hillman, R. A. McLaughlin, B. C. Quirk, and D. D. Sampson, "*In vivo* dynamic optical coherence elastography using a ring actuator," *Opt. Express* **17**(24), 21762–21772 (2009).
21. X. Liang and S. A. Boppart, "Biomechanical properties of *in vivo* human skin from dynamic coherence elastography," *IEEE Trans. Biomed. Eng.* **57**(4), 953–959 (2010).
22. X. Liang, S. G. Adie, R. John, and S. A. Boppart, "Dynamic spectral-domain optical coherence elastography for tissue characterization," *Opt. Express* **18**(13), 14183–14190 (2010).
23. S. G. Adie, X. Liang, B. F. Kennedy, R. John, D. D. Sampson, and S. A. Boppart, "Spectroscopic optical coherence elastography," *Opt. Express* **18**(25), 25519–25534 (2010).
24. R. Leitgeb, L. Schmetterer, W. Drexler, A. F. Fercher, R. J. Zawadzki, and T. Bajraszewski, "Real-time assessment of retinal blood flow with ultrafast acquisition by color Doppler Fourier domain optical coherence tomography," *Opt. Express* **11**(23), 3116–3121 (2003).
25. R. Leitgeb, C. K. Hitzenberger, and A. F. Fercher, "Performance of fourier domain vs. time domain optical coherence tomography," *Opt. Express* **11**(8), 889–894 (2003).
26. J. F. de Boer, B. Cense, B. H. Park, M. C. Pierce, G. J. Tearney, and B. E. Bouma, "Improved signal-to-noise ratio in spectral-domain compared with time-domain optical coherence tomography," *Opt. Lett.* **28**(21), 2067–2069 (2003).
27. M. Wojtkowski, T. Bajraszewski, P. Targowski, and A. Kowalczyk, "Real-time *in vivo* imaging by high-speed spectral optical coherence tomography," *Opt. Lett.* **28**(19), 1745–1747 (2003).
28. N. Nassif, B. Cense, B. Park, M. Pierce, S. Yun, B. Bouma, G. Tearney, T. Chen, and J. de Boer, "*In vivo* high-resolution video-rate spectral-domain optical coherence tomography of the human retina and optic nerve," *Opt. Express* **12**(3), 367–376 (2004).
29. T. A. Krouskop, T. M. Wheeler, F. Kallel, B. S. Garra, and T. Hall, "Elastic moduli of breast and prostate tissues under compression," *Ultrason. Imaging* **20**(4), 260–274 (1998).
30. B. H. Park, M. C. Pierce, B. Cense, S.-H. Yun, M. Mujat, G. J. Tearney, B. E. Bouma, and J. F. de Boer, "Real-time fiber-based multi-functional spectral-domain optical coherence tomography at 1.3 microm," *Opt. Express* **13**(11), 3931–3944 (2005).
31. J. D'hooge, A. Heimdal, F. Jamal, T. Kukulski, B. Bijnens, F. Rademakers, L. Hatle, P. Suetens, and G. R. Sutherland, "Regional strain and strain rate measurements by cardiac ultrasound: principles, implementation and limitations," *Eur. J. Echocardiogr.* **1**(3), 154–170 (2000).
32. T. Gambichler, G. Moussa, M. Sand, D. Sand, P. Altmeyer, and K. Hoffmann, "Applications of optical coherence tomography in dermatology," *J. Dermatol. Sci.* **40**(2), 85–94 (2005).
33. H. Fruhstorfer, U. Abel, C.-D. Garthe, and A. Knüttel, "Thickness of the stratum corneum of the volar fingertips," *Clin. Anat.* **13**(6), 429–433 (2000).
34. "Fiji is just ImageJ," <http://pacific.mpi-cbg.de/wiki/index.php/>.
35. S. I. O'Donoghue, A.-C. Gavin, N. Gehlenborg, D. S. Goodsell, J.-K. Hériché, C. B. Nielsen, C. North, A. J. Olson, J. B. Procter, D. W. Shattuck, T. Walter, and B. Wong, "Visualizing biological data—now and in the future," *Nat. Methods* **7**(3), S1–S4 (2010).
36. A. Limaye, "Drishti-volume exploration and presentation tool," IEEE Visual., Baltimore, USA (2006).
37. R. O. Potts, D. A. Chrisman, Jr., and E. M. Buras, Jr., "The dynamic mechanical properties of human skin *in vivo*," *J. Biomech.* **16**(6), 365–372 (1983).
38. A. Gabrielli, E. V. Avvedimento, and T. Krieg, "Scleroderma," *N. Engl. J. Med.* **360**(19), 1989–2003 (2009).
39. J. De Rigal, and J. L. Leveque, "*In vivo* measurement of the stratum corneum elasticity," *Bioeng. Skin* **1**, 13–23 (1985).

40. F. M. Hendriks, D. Brokken, C. W. J. Oomens, and F. P. T. Baaijens, "Influence of hydration and experimental length scale on the mechanical response of human skin *in vivo*, using optical coherence tomography," *Skin Res. Technol.* **10**(4), 231–241 (2004).
 41. S. Makita, Y. Hong, M. Yamanari, T. Yatagai, and Y. Yasuno, "Optical coherence angiography," *Opt. Express* **14**(17), 7821–7840 (2006).
 42. A. Szkulmowska, M. Szkulmowski, A. Kowalczyk, and M. Wojtkowski, "Phase-resolved Doppler optical coherence tomography—limitations and improvements," *Opt. Lett.* **33**(13), 1425–1427 (2008).
-

1. Introduction

It is well known that pathological tissue is often stiffer than healthy tissue [1]. Much research has focused on using the elastic properties of tissue as a contrast mechanism to form images, a technique known as elastography [2,3]. Initial elastography techniques used ultrasound [4] and magnetic resonance imaging (MRI) [5] as the underlying imaging modalities and *in vivo* elastography has been proposed for clinical applications in the diagnosis of breast cancer [6,7], prostate cancer [8], cirrhosis of the liver [9], brain tumors [10] and atherosclerosis [11].

The first optical elastography to have been developed is optical coherence elastography (OCE), which uses optical coherence tomography (OCT) as the underlying imaging modality [12–23]. The spatial resolution of OCE, as set by OCT, is typically 1–10 μm ; at least an order of magnitude higher than ultrasound- and MRI-based elastography. OCE has been proposed for application in dermatology [12,19–21], atherosclerosis [13,14], tissue engineering [15], and tumor margin [18,22,23]. The ability to perform routine *in vivo* measurements is a key prerequisite for the clinical application of OCE. To date, however, there have been only three demonstrations of *in vivo* OCE imaging [12,19,20]. In the first, *in vivo* images of human skin were recorded with a TD-OCT system at maximum line rates of 11 Hz [12]. Due to the large preload applied, at least one minute was required to allow internal strain dissipation prior to imaging. More recently, an audio-frequency sub-micron excitation technique has been reported, which overcame the need to allow strain dissipation [19,20]. It was also demonstrated on human skin using a TD-OCT system, and the line rate was limited to ~ 1 Hz. Such long acquisition times are impractical for *in vivo* imaging in a clinical setting and result in large motion artifacts.

In this paper, we perform for the first time *in vivo* OCE imaging using a spectral-domain OCT (SD-OCT) system. This technique, similar to Doppler SD-OCT [24], is based on a dynamic OCE technique recently proposed [22]. Here, we report its operation at a line rate of 5 kHz; >450 times higher than *in vivo* OCE imaging reported to date. The use of SD-OCT provides rapid acquisition whilst maintaining high signal-to-noise [25,26], thus, enabling three-dimensional (3D) imaging [27,28]. 3D imaging of such features as pathological regions of tissue has the potential to greatly increase the utility and impact of OCE in a clinical setting. We combine this approach with two key practical requirements required for *in vivo* imaging. We employ a ring actuator sample arm [20], enabling mechanical excitation to be introduced to tissue from the same side as the OCT beam. Using a custom-built force sensor, we apply a controlled preload to tissue to avoid the large variations in strain that have been reported as a function of preload [29]. Constant preload is important if an accurate comparison is to be made between images recorded from different locations. We demonstrate *in vivo* 3D-OCE imaging on both normal and hydrated skin and report a more elastic response of the stratum corneum in hydrated skin.

2. Experimental setup

The 3D-OCE system reported here is based on an SD-OCT system operating with line rate of 5 kHz and B-scan rate in the range 0.7–2.5 Hz. A schematic diagram of the system is presented in Fig. 1(a). The optical source comprised a Nd:YVO₄-pumped titanium-sapphire laser (pulse width ~ 100 fs, repetition rate 80 MHz), with a center wavelength of 800 nm and a 3 dB bandwidth of 100 nm, providing a theoretical axial resolution of 2.8 μm . The average power incident on skin was 7 mW. The sample arm contained a triplet lens to focus the optical

beam through a 2 mm-thick glass window fixed to the surface of a piezoelectric ring actuator. This arrangement provided a theoretical lateral resolution of 15 μm . Lateral scanning was performed using a Scancube[®]7 (Scanlab AG, Puchheim, Germany) *x-y* galvanometer mirror pair. The spectrometer consisted of a 100 mm-focal-length lens, an 830 lines/mm diffraction grating, and a CCD line camera (1024 pixels). Data were recorded on a PC with a 3.2 GHz Intel Xeon processor and 2 GB of RAM. The measured sensitivity was 94 dB at a depth of 280 μm , rolling off to 81 dB at a depth of 1 mm and the axial measurement range was 2 mm. The phase noise was measured to be 53 mrad, for an SNR of 44 dB. The phase noise was calculated using a method described previously [30].

Dynamic uni-axial compressive loading was applied to skin by bringing it into contact with the ring actuator. The glass window compressed the skin against the underlying bone, which acted as a rigid body, operating from the same side as the illumination beam. The ring actuator had an aperture of 9 mm, maximum stroke of 12 μm , stiffness of 250 N/ μm and resonance frequency of 45 kHz. A sinusoidal excitation signal was introduced to skin with unloaded amplitude in the range 1-6 μm and frequency in the range 50-250 Hz. No variation in skin elasticity was measured over these ranges. Given this observation, an amplitude of 4 μm and frequency of 125 Hz were arbitrarily chosen for all subsequent measurements.

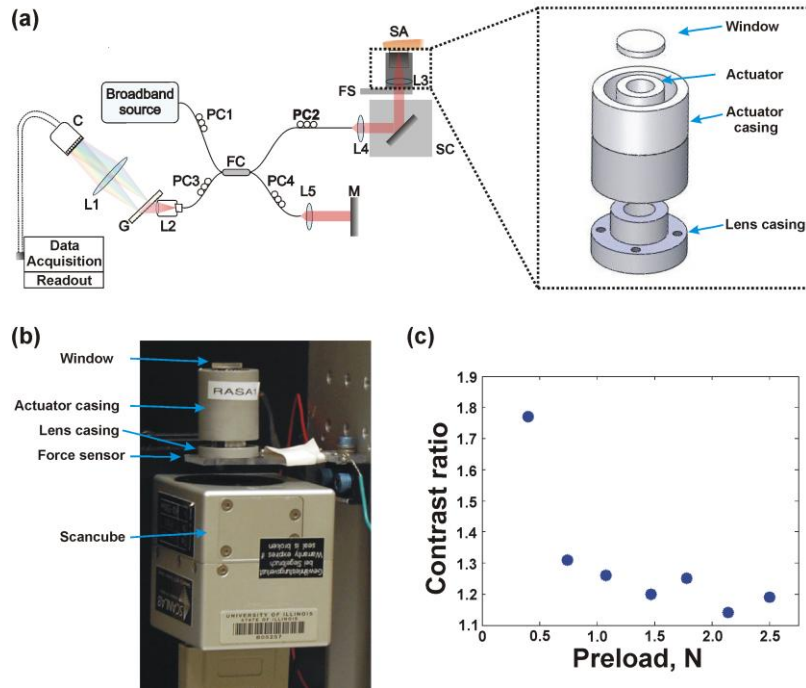


Fig. 1. (a) Schematic diagram of the OCE system; C: CCD camera, L1-L5: lenses, G: diffraction grating, PC1-PC4: polarization controllers, FC: 50/50 fiber coupler, M: mirror, FS: force sensor, SC: Scancube, SA: sample arm. A schematic of the sample arm is presented in the inset; (b) Photograph of the sample arm; and (c) Contrast ratio (ratio of strain rate magnitude) between stratum corneum and epidermis versus preload.

A schematic of the ring actuator sample arm is presented in the inset of Fig. 1(a). The lens, ring actuator and glass window were fixed in a two-section aluminum casing of 30 mm diameter and 45 mm total height. The lens was fixed in the first section and the ring actuator was fixed to the base of the second section using epoxy. The two sections were coupled with an adjustable thread allowing the beam to be focused to different depths within the sample. A photograph of the sample arm is presented in Fig. 1(b).

The preload applied was measured using a custom-built polycarbonate cantilever force sensor fixed to the lens casing and with a 10-mm clear aperture, illustrated in Fig. 1(a) and seen in Fig. 1(b). The change in resistance of strain gages glued to the polycarbonate surface was used to determine the applied force. The force sensor had a measured accuracy of 0.1 N. The preload applied to skin was varied in the range 0.4-2.5 N; the lower value corresponded to the minimum force that could be maintained. To select the optimum preload, the mean strain rate magnitude, defined in Section 3, was calculated in a homogenous area of $60 \mu\text{m} \times 75 \mu\text{m}$ in both the stratum corneum (area 1) and the living epidermis (area 2). The contrast ratio, CR , was then calculated as a function of preload: $CR = |\varepsilon_m|_{\text{area2}}/|\varepsilon_m|_{\text{area1}}$, where $|\varepsilon_m|$ is the strain rate magnitude calculated in each homogenous area. The results are presented in Fig. 1(c). A maximum contrast ratio of 1.8 was obtained for the minimum applied preload (0.4 N), which was subsequently used to obtain all results presented in this paper. This value is consistent with previous *in vivo* OCE measurements [19,20].

3. Experimental method

The method used to generate OCE B-scan images has been presented in detail previously [22], so only a brief description is provided here. OCT B-scans of skin were recorded during external dynamic excitation. Local skin displacement as a function of depth was determined at each lateral position by calculating the phase difference, $\Delta\phi$, between consecutive A-scans, resulting in a 2D phase-difference map modulated at the excitation frequency. To generate OCE images, strain rate was calculated. Strain rate, ε_m (s^{-1}), is the rate at which deformation occurs and is commonly used in presenting images in ultrasound elastography [31], as well as in OCE [16,17,22], in order to differentiate tissues based on elastic properties. It may be defined as:

$$\varepsilon_m'(z,t) = \frac{1}{z_0} \frac{\Delta d}{\Delta t} = \frac{\Delta\phi(z,t)\lambda}{4\pi n \Delta t z_0}, \quad (1)$$

where Δd is the displacement and Δt is the time interval between successive A-scans, λ is the mean wavelength of the light source, n is the refractive index of the sample, assumed to be 1.4 for human skin, and z_0 is the original thickness of the sample. For measurements of the fingertip, z_0 is the distance to the underlying bone, assumed to be 2 mm in the results presented here [12].

In the technique reported here, the value of each pixel in an image is equal to the strain rate magnitude introduced to the sample at that location [22]. Each pixel, therefore, represents one excitation cycle. To optimize the OCE axial resolution, Δz_{OCE} , the excitation amplitude should be less than the OCT axial resolution. The OCE lateral resolution, Δx_{OCE} , corresponds to the distance scanned by the optical beam in one excitation cycle. It may be defined as the ratio of lateral scan range, SR_l , to the number of excitation cycles, P_N , introduced in one B-scan. For optimum resolution, this ratio should be less than the lateral resolution of the OCT system:

$$\frac{SR_l}{P_N} < \Delta x_{\text{OCT}}, \quad (2)$$

where Δx_{OCT} corresponds to the OCT system lateral resolution. P_N in Eq. (2) also determines the OCE B-scan acquisition time. For example, in the OCE results presented in Fig. 3 below, 175 excitation cycles were introduced across a lateral range of 2 mm. For an excitation frequency of 125 Hz, this corresponds to a B-scan acquisition time of 1.4 s. In Fig. 2(a), a strain rate image measured from human skin *in vivo* is presented. Modulation of the strain rate image due to dynamic excitation at 125 Hz is visible. In Fig. 2(b), a plot of the strain rate introduced at a depth of 150 μm , indicated by the black line in (a), is presented. The OCE

image resolution is determined by measuring the amplitude (axial resolution) and period (lateral resolution) of this modulation, as illustrated in Fig. 2(c).

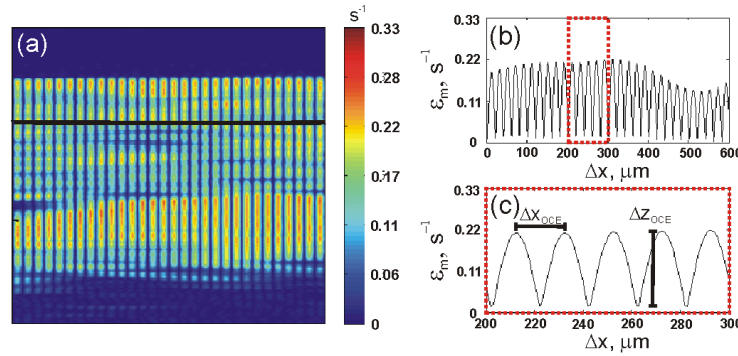


Fig. 2. Axial and lateral resolution of OCE images. (a) Strain rate image recorded on human skin *in vivo* (image dimensions (x - z) are $600 \mu m \times 800 \mu m$); (b) Strain rate measured at depth $150 \mu m$, indicated by black line in (a); (c) Highlighted region of (b) indicating how axial and lateral resolutions in OCE images are determined.

A lateral displacement of the probing light beam in the range 0.2 - $1 \mu m$ was introduced between each A-scan. This oversampling with respect to the lateral resolution of the OCT system minimized phase error due to lateral scanning. The phase error is also dependent on the SNR of the OCT signal [30]. The excitation frequency and amplitude selected ensured the phase difference caused by sample motion between A-scans was always less than $|\pi|$, setting an upper limit for strain rate measurement of $\sim 0.35 s^{-1}$. In regions of the image with low SNR, phase wrapping errors can lead to inaccurate measurement of strain rate. To ameliorate this problem, we thresholded the OCT signal prior to calculating the phase difference [17], using a threshold of 10 dB above the noise floor. This corresponds to a phase sensitivity of 0.3 rad and a minimum measurable strain rate of $0.03 s^{-1}$. A digital 30 -Hz band-pass filter centered at the excitation frequency of 125 Hz was applied to the phase difference data to further reduce noise.

In all results presented in Section 4, the OCT and OCE images were generated from the same complex OCT data sets acquired under mechanical excitation. This minimized acquisition time and ensured that each pair of OCT and OCE images were recorded from the same region of tissue.

4. Results

In Figs. 3(a) and 3(b), OCT and OCE images of skin from the tip of the middle finger of a 29-year-old male are presented. For both images, the acquisition time was 1.4 s and the number of pixels in the z -direction is 700 . The number of pixels in the x -direction in Fig. 3(a) is $7,000$; determined by the number of A-scans recorded per B-scan, and 175 in Fig. 3(b); determined by the number of excitation cycles. Dense sampling in the x -direction was chosen to minimize phase errors due to lateral scanning. To reduce noise, a median filter (7×3 kernel) was applied. For the OCE data, it was applied following thresholding and prior to extraction of the strain rate magnitude. The unequal kernel size is to account for different pixel numbers in the x and z directions. In Fig. 3(a), the glass imaging plate, stratum corneum and living epidermis are labeled. The stratum corneum is the lower scattering, more superficial layer of the epidermis and the living epidermis is the higher scattering, deeper region consisting of papillary ridges. Strong contrast is observed between the stratum corneum and the living epidermis. The stratum corneum has a thickness, in optical pathlength, of approximately $300 \mu m$, consistent with previous OCT measurements [32,33]. A sweat gland is also present, indicated by higher signal intensity than the surrounding stratum corneum. The OCE image

recorded from the same region is presented in Fig. 3(b). In Fig. 3(c), the OCE signal (color map) is overlaid on the OCT signal (grayscale). Due to the OCE signal density, only the top 40% of the OCE signal is presented, so that the underlying OCT signal is visible. Contrast between the stratum corneum and the living epidermis is visible in all images. The strain rate magnitude on average is higher in the living epidermis than in the stratum corneum, suggesting it has a more elastic response, as previously reported [12,19–21]. Although there are subtle differences in the two images, in general, the strain rate magnitude tracks proportionally the OCT image signal intensity. We speculate that this is because higher optical scattering areas are more dense [32,33] and, therefore, stiffer. It should be noted that higher optical scattering may also be caused by differences in refractive index.

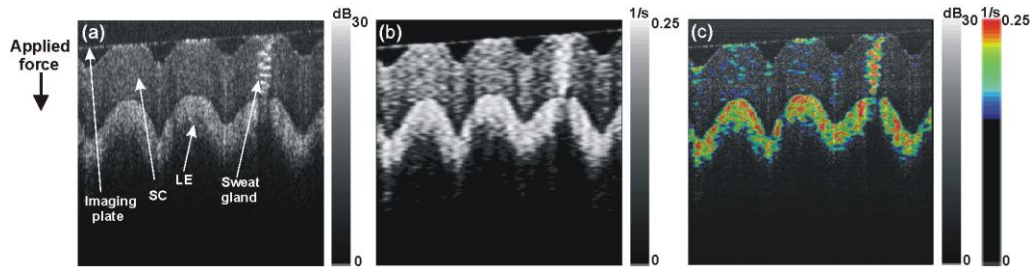


Fig. 3. (a) OCT; (b) OCE; and (c) overlaid images of *in vivo* skin on the middle finger. In (a), the stratum corneum (SC), living epidermis (LE), imaging plate and a sweat gland are labeled. Image dimensions are $1.4 \text{ mm} \times 1.4 \text{ mm}$.

A significant improvement in OCE image resolution is visible in Fig. 3 in comparison to *in vivo* OCE images previously presented [12,19,20]. This is largely due to the faster acquisition speed obtained by using the SD-OCT system, which results in significantly reduced motion artifacts.

3D-OCT and OCE images of skin from the middle finger of the same subject are presented in Fig. 4. OCE B-scans at each y -position were generated using the technique described above. The total acquisition time for a 3D-OCE data set was 5 min for images with dimensions (xyz) of $2 \text{ mm} \times 1 \text{ mm} \times 1 \text{ mm}$. To reduce motion artifacts, the finger was strapped in position prior to each measurement. To keep the acquisition time as short as possible, only 50 excitation cycles per B-scan were used; reducing the B-scan acquisition time to 0.4 s. This was achieved by reducing the number of A-scans per B-scan from 7,000 to 2,000; resulting in a lateral resolution of $40 \mu\text{m}$ in the x -direction. The reduction of spatial resolution is visible in Fig. 4. In the z -direction, there are 1,024 pixels and in the y -direction, 100 pixels (1-mm range). The raw OCE and OCT data sets were cropped and transformed within an image processing package [34] and then normalized so that the intensity range was 0.0-1.0 [35]. The data sets were then imported into a volume exploration and presentation tool [36], and reconstructed into 3D data sets at full resolution. The corresponding visualizations were produced from view-aligned, slice-based rendering. Final pixel contributions were defined by applying a two-dimensional transfer function that weighted the opacity and color of each voxel based on the intensity and gradient value in the volumetric data sets.

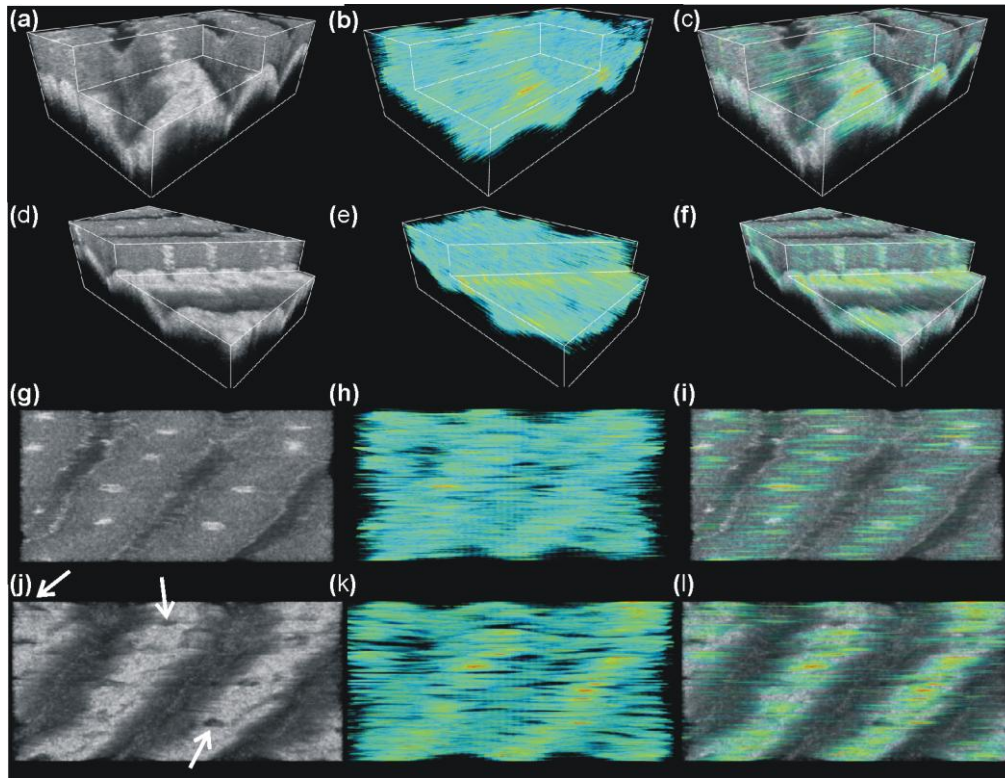


Fig. 4. 3D visualization of *in vivo* skin from the middle finger of a male subject. (a) OCT, (b) OCE, and (c) overlay, from first perspective view; (d) OCT, (e) OCE, and (f) overlay, from second perspective view; (g) OCT, (h) OCE and (i) overlay, from *en face* view of skin surface; (j) OCT, (k) OCE and (l) overlay, from *en face* view at depth of 300 μm . The arrows in (j) indicate shadow artifacts due to overlying sweat glands. Volume dimensions (xyz) are 2 mm \times 1 mm \times 1 mm. Full 3D data sets also available, [View 1](#) (OCT) and [View 2](#) (OCE).

In Figs. 4(a) and 4(d), two perspective views of the OCT data are presented, with one corner cut away to a depth of 300 μm , revealing internal structure. In Figs. 4(b) and 4(e), the OCE signal is displayed and, in Figs. 4(c) and 4(f), the OCE data is overlaid on the OCT data, as in Fig. 3(c). In these images, the highest OCE signal is visible in the living epidermis and the sweat glands, consistent with the result presented in Fig. 3. In Figs. 4(g)-4(i) *en face* views from the surface of the tissue are presented. In the OCT image, presented in Fig. 4(g), sweat glands are visible as regions of high signal intensity. Large variations in the strain rate magnitude are visible in Fig. 4(h) in the regions corresponding to sweat glands in Fig. 4(g). Additional regions of high OCE signal in Fig. 4(h) may correspond to sweat glands not visible in the OCT data. The OCE signal overlaid on the OCT signal is presented in Fig. 4(i). A second *en face* view is presented in Figs. 4(j)-4(l) at a depth of 300 μm . The regions of high OCT signal at this depth correspond to the living epidermis. Shadows of the sweat glands are visible in Fig. 4(j). Several of these shadow artifacts are indicated in the figure (white arrows). In the OCE images presented in Fig. 4(k), the living epidermis is represented by regions of high OCE signal. This is consistent with the result presented in Fig. 3. The OCE signal overlaid on the OCT signal is presented in Fig. 4(l). The full 3D data sets are also available, [View 1](#) (OCT) and [View 2](#) (OCE).

The skin on the middle finger of the same subject was hydrated in warm water for 30 min and then imaged with the same acquisition settings, preload, excitation amplitude and frequency, and median filtering as for the images presented in Fig. 3. An OCT image of the hydrated skin is presented in Fig. 5(a). The imaging plate, stratum corneum and living

epidermis are readily distinguished. The OCE image is presented in Fig. 5(b). The contrast between stratum corneum and living epidermis is reduced in comparison to the results presented in Fig. 3(b). This is attributed to a more elastic response of the stratum corneum in the hydrated case [37]. An artifact is visible in Fig. 5 – the surface of the imaging plate appears not to be perfectly flat. We believe that this is caused by a variation in the thickness of the index-matching glycerol used, which results in a slight variation in the optical path length. As in Fig. 3(c), in Fig. 5(c) the top 40% of the OCE signal (color map) is overlaid on the OCT signal (grayscale).

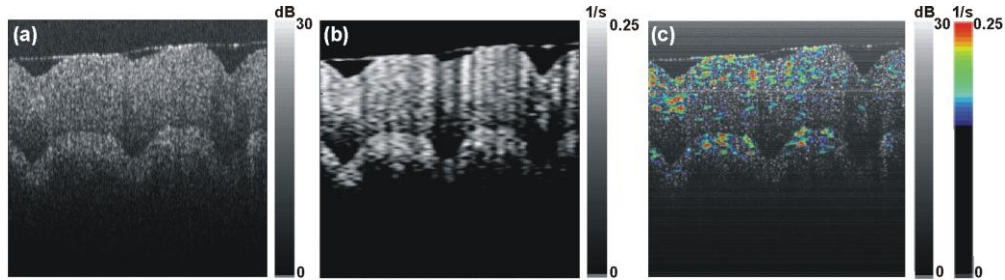


Fig. 5. (a) OCT; (b) OCE; and (c) overlaid images of the *in vivo* hydrated skin on the middle finger. Image dimensions are 1.4 mm \times 1.4 mm.

3D-OCT and OCE imaging were also performed on the hydrated skin and are presented in Fig. 6. In the hydrated 3D-OCE case, 250 excitation cycles were introduced across a lateral range of 2 mm, compared with 50 excitation cycles across the same distance in Fig. 4. This resulted in the lateral resolution in the x -direction being determined by the lateral resolution of the OCT system. The trade-off is that the acquisition time increased by a factor of five, resulting in an acquisition time of 25 min, and motion artifacts became more prominent and were manifested by geometrical distortion of skin features.

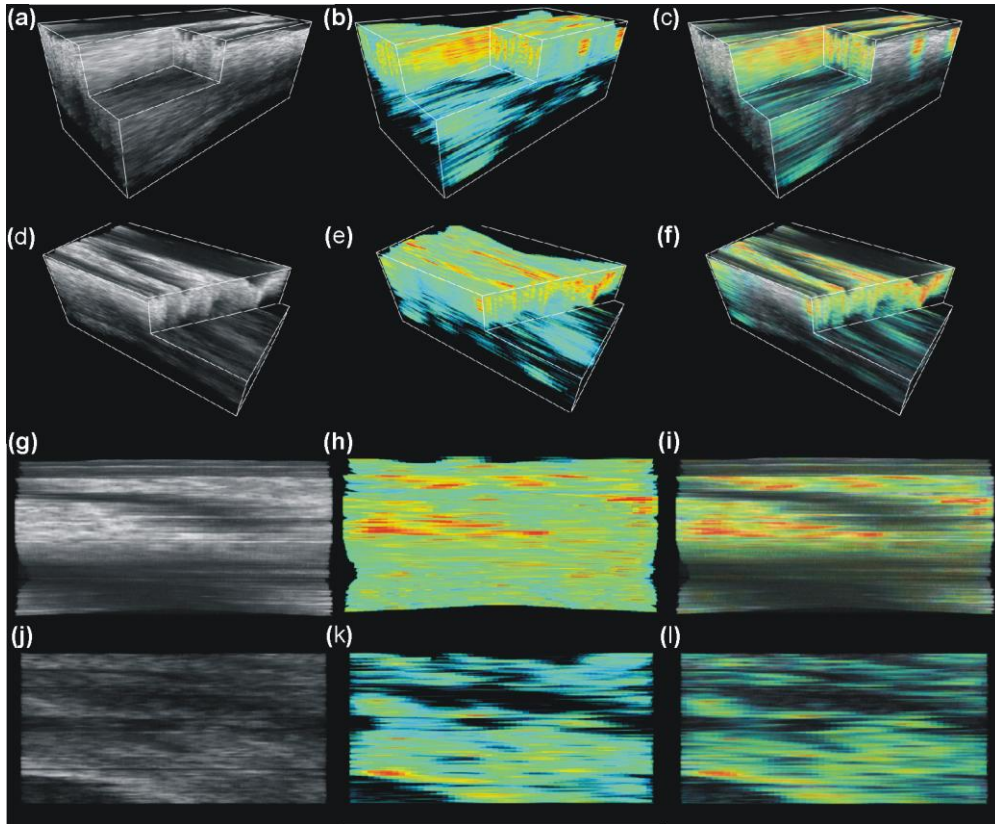


Fig. 6. *In vivo* 3D visualizations of hydrated skin from the middle finger of a male subject. (a) OCT, (b) OCE, and (c) overlay, from first perspective view; (d) OCT, (e) OCE, and (f) overlay, from second perspective view; (g) OCT, (h) OCE and (i) overlay, from *en face* view of skin surface; (j) OCT, (k) OCE and (l) overlay, from *en face* view at depth of 300 μm . Volume dimensions (xyz) are 2 mm \times 1 mm \times 1 mm. Full 3D data sets also available, [View 3](#) (OCT) and [View 4](#) (OCE).

In a similar manner to the results presented in Figs. 4(a) and 4(d), in Figs. 6(a) and 6(d) perspective views of the OCT data from the hydrated skin are presented, with one corner cut away to a depth of 300 μm , revealing internal structure. In Figs. 6(b) and 6(e), the OCE signal is displayed and, in Figs. 6(c) and 6(f), the OCE data is overlaid on the OCT data. On average the OCE signal is higher in the hydrated stratum corneum when compared with the unhydrated stratum corneum shown in Figs. 4(b) and 4(e), suggesting a more elastic response. In Figs. 6(g)-6(i), *en face* views from the surface of the tissue are presented. In comparison to Fig. 4(g), the hydrated *en face* OCT image from the skin surface (Fig. 6(g)) appears relatively uniform. The sweat glands are not visible in the hydrated case. However, large variations in the OCE image are visible in Fig. 6(h). We speculate that this is due to variations in the hydration state of the skin. A second *en face* view is presented in Figs. 6(j)-6(l) at a depth of 300 μm . Large variations in the OCE signal, possibly due to changes in hydration level, are also visible at this depth. The full 3D data sets are also available, [View 3](#) (OCT) and [View 4](#) (OCE).

5. Discussion

The results presented confirm the ability to perform high-resolution, 3D imaging of the elastic properties of the superficial skin *in vivo*. Using elastic properties as a contrast mechanism may increase the potential to detect pathological tissues. The application of OCT to dermatology

has great potential in clinical application and medical research [32,33]. OCE could provide images of the elastic properties of skin with comparable resolution. Such measurements could be of particular use in the diagnosis and treatment of scleroderma [38], for example. The increased strain of the stratum corneum in the hydrated case has been previously reported based on both non-optical [39] and OCT measurements [40]. Previous OCE measurements have shown a more elastic response of the epidermis in comparison to the stratum corneum [12,19,20]. The observed more elastic response of the stratum corneum in the hydrated case is consistent with previous reports [37]. However, in [37], the authors measured the propagation and attenuation of low-amplitude surface waves on the skin rather than the strain.

In OCE results presented to date, both the strain and the strain rate have been used to quantify the elastic properties of samples. In this paper, we presented strain rate images, consistent with recent reports on OCE [17,18,22]. Since strain rate is the time rate of change of strain, the strain may be determined from it by integration over time.

As discussed in Section 2, the maximum achievable acquisition speed for OCE measurements is limited by the excitation frequency used. For the images presented in Fig. 3, the B-scan acquisition time was 1.4 s, as 175 excitation cycles were recorded at 125 Hz. By increasing the excitation frequency to 800 Hz, as used in previous *in vivo* OCE studies [19,20], the acquisition time for the data generated in Fig. 3 would be reduced to 0.2 s. The acquisition speed can also be increased by scanning over smaller ranges, reducing the number of excitation cycles required to satisfy Eq. (2). The 3D images presented in Figs. 4 and 6 highlight the coupling between the number of excitation cycles introduced per B-scan and the lateral resolution of the resulting OCE image. Faster acquisition time was achieved at the expense of degraded lateral resolution (Fig. 4). Conversely, higher lateral resolution was achieved at acquisition times that resulted in motion artifacts (Fig. 6). Improvements to acquisition time and lateral resolution, whilst minimizing motion artifacts, will be the subject of future investigations. The techniques developed to remove the effects of artifacts caused by bulk motion in OCT flow measurements [41] should apply to OCE.

Minimizing the impact of phase noise is an important consideration for OCE processing. In regions where the magnitude of the phase difference between A-scans is close to π , the addition of phase noise can result in phase wrapping errors that shift the effective frequency content of the vibration signal. In practice, the problem of phase wrapping induced by noise when the phase difference is close to π can be addressed by increasing the A-scan rate or reducing the actuator drive amplitude. Since phase noise increases with decreasing SNR, we utilized an SNR threshold as in [17], in which velocities corresponding to low SNR pixels were set to zero. Future investigations will examine post-processing techniques to minimize the impact of phase noise for large vibration amplitudes, particularly in regions with low SNR. In future work, we will also investigate using averaging and filtering techniques previously developed for Doppler OCT flow measurements [42].

The use of the force sensor demonstrated here is important because it enables repeatable measurements to be performed and ensures that the elastic properties of different samples are investigated under the same preload. Notably, large variations in the measured strain in tissues have been reported for relatively moderate increases in preload [29]. For *in vivo* skin measurements, comparable results were obtained on several subjects, as well as on the same subject on different days (data not presented).

The ring actuator sample arm presented in this work could be used as the basis for a handheld probe for use *in vivo*. This could be readily achieved by fixing the cantilever force sensor to the scan cube casing.

6. Conclusions

We have presented the first 3D-OCE images. Experiments were performed on *in vivo* human skin with a constant preload applied by a custom-built ring actuator and integrated force sensor. Use of an SD-OCT system for image acquisition allowed >450-times higher line rate

than previously reported for *in vivo* OCE imaging. 3D-OCE data, processed in 2D and displayed in 3D, were presented for both normal and hydrated human skin. OCE images showed strong correlation with the underlying OCT images. The strain rate of the hydrated stratum corneum was measured to be higher than that of the unhydrated stratum corneum, confirming a more elastic response, as expected. The results in this paper support the continued investigation of OCE as a technique for probing the elastic properties of tissue *in vivo*.

Acknowledgements

We would like to acknowledge the technical contributions of Dr. Robert McLaughlin, Dr. Haohua Tu, Dr. Renu John, Vasilica Crecea, and Yuan Liu to this paper. B.F.K. acknowledges funding support from a UWA Research Collaboration Award. This research was supported in part by grants from the National Institutes of Health (1 RC1 CA147096, S.A.B.) and the National Science Foundation (CBET 08-52658 ARRA, S.A.B.).